Journal of Geophysical Research (Solid Earth)

Supporting Information for

Postseismic Relocking of the Subduction Megathrust Following the 2007 Pisco, Peru earthquake

D.Remy [(a)], H.Perfettini[(b)], N.Cotte[(b)], J.P Avouac[(c)], M. Chlieh[(d)], F. Bondoux[(a)], A. Sladen[(d)], H. Tavera[(e)], A. Socquet[(b)]

[(a)] GET / UMR5563 (UPS, CNRS, IRD, CNES); Obs. Midi-Pyrénées, Université P. Sabatier, Toulouse, France.

[(b)] ISTERRE / UMR5275 (UJF, CNRS, IRD); Obs. des Sciences de l'Univers de Grenoble, Université Joseph Fourier, Grenoble, France

[(c)] Division of Geological and Planetary Science, California Institute of Technology, Pasadena, CA, USA.

[(d)]GEOAZUR / UMR7329 (UNSA, CNRS, IRD) ; Obs. de la Côte d'Azur, Université Nice-Sophia Antipolis, Valbonne, France

[(e)]Instituto Geofísico del Perú, Calle Badajos 169, Urb. Mayorazgo, Ate, Lima, Perú

Contents of this file

Introduction

Section text S1 presents a comparison between InSAR and GPS data. Section Text S2 presents different resolution tests for the co, post and interseismic models considering each dataset used in this study. Section Text S3 presents the analysis of the variation of the χ^2_r of the residuals between the observed and the reconstructed GPS time series. Section Text S4 details the approach used in this study to determine the optimal value of the smoothing parameter. The coseismic distribution model used in the study is described in section Text S5. In section Text S6 we discuss the robustness of the existence of the region with afterslip reversal in our best postseismic slip distribution model displayed in Figures 6, 7 and 9. In section Text S7 we present the calculation leading to the estimate of the total postseismic moment.

Text S1. Comparison between data sets

In this section, InSAR and GPS measurements are compared. Out of 5 stations, 2 stations lie inside the ENVISAT track 354 and the ALOS track 111 interferograms (LAGU and ENAP) and one inside the ALOS track 110 interferogram (GUAD). Table S1 lists the values of the displacement in the LOS direction observed by GPS and by InSAR. For the ALOS track 111 interferograms, the comparison between GPS and InSAR is made using the GPS observation day 14 whereas the master image used to form the ALOS track 111 interferograms was

acquired 12 days after the earthquake because the continuous GPS measurements at ENAP began 14 days after the earthquake (the complete network of 5 stations was fully operational 20 days after the mainshock). The difference between measurements derived from GPS InSAR data is ~0.5 cm for ENVISAT and ~1 cm for ALOS. This difference, of the same order of magnitude than the estimated noise of the interferograms, shows the good consistency between the two data sets. Only stations GUAD and LAGU still continue to provide continuous observations in the study area. GPS data are collected approximately every year at other stations in campaign mode.

Text S2. **Resolution Tests for the Co, Post- and Interseismic Slip Distributions**

We present here resolution tests for the co-, post- and interseismic models considering each dataset used in this study. An initial slip distribution consisting of a collection of circular asperities (35 km for the co- and postseismic model and 70 km for the interseismic one) with unit slip is built. The resulting surface deformation is then computed at the location of the GPS and InSAR observation sites and inverted to obtain the corresponding slip distribution. The azimuth of slip is fixed to 200°SSW for the co- and the postseismic models and 20°NNW for the interseismic one. Different values of γ are considered.

For the co- and postseismic models, the initial distribution is well recovered except in the north-west corner of the fault where smooth models fail to resolve the imposed slip distribution (Figures S3a and S3b). For the interseismic case (Figure S3c), the imposed slip distribution is properly recovered. Not surprisingly, rough models always allow a better reconstruction of the initial slip distribution.

Text S3. Choice of the Number of Components for the PCAIM Decomposition

To determine the number of components needed to properly reconstruct the dense GPS data set, we compute the reduced Chi-square χ^2_r (Eq. 2) between the data and the decomposition results considering an increasing number of components.

Figure S4 plots χ^2_r as a function of the number of components of the PCAIM decomposition, showing that χ^2_r decreases from 5.24 to 0 as the number of components is increased. This figure shows that using four components is enough to reconstruct the data within uncertainties.

Figure S5 shows the four eigenvectors describing the temporal evolution of the time series. The eigenvector $\boldsymbol{V_1}$ corresponding to the largest eigenvalue initially increases as the logarithm of time before reaching a near constant value. It might be interpreted as the net postseismic motion. The second eigenvector $\boldsymbol{V_2}$ start to increase as the logarithm of time before decaying roughly linearly with time. Figure 3, displaying the GPS time series, shows that this component alone describes the return to the interseismic phase. Finally, the last two components show oscillatory motions with zero mean. As the period of the oscillations are annual, they describe seasonal variations in the cGPS time series.

The second eigenvector $\boldsymbol{V_2}$ shows an anomalous behavior between days 70 and 220. This comes from the fact that 4 out of 5 stations were not operational in this time period. Therefore, the decomposition in this time period is only constrained by station LAGU and the results become noisy. To correct this effect, we fit $\boldsymbol{V_2}$ using Eq. (50) of *Perfettini and Avouac* [2004]. The values of $\boldsymbol{V_2}$ from day 70 to 220 are further replaced (red line of the V_2 plot of Figure S5) by the values of the best fit. No further modification is applied on the rest of the temporal eigenvectors.

Text S4. Choice of the Optimal Smoothing Parameter

In this section, we look for the optimal value of the smoothing parameter for each slip model. The weight put on smoothing is found based on the L-curve [*Hansen*, 1992; *Hansen and O'Leary*, 1993]. All models have a fix slip azimuth (N250°E) for the co- and postseismic models and N70°E for the interseismic model).

Figure S6 shows, for the coseismic model, the moment and reduced chi-square as a function of the smoothing parameter. Our optimal model corresponds to γ=2. We define the range of acceptable models such that the rougher of our models corresponds to γ=0.2 while γ=20 for the smoother model. All acceptable models show the existence of an asperity located west of the Paracas Peninsula.

Postseismic models are computed for three roughness values encompassing three orders of magnitude of the smoothing parameter (2.5×10^2 , 2.5×10^3, 2.5×10^4). Figure S7 shows the moment and reduced chi-square as a function of the smoothing parameter. The smoother model poorly explains the data (χ^2 of ~5) while the roughness and the optimal models are acceptable models ($\chi^2 < 1$). The three models predict that most afterslip (region A) is located south of the fault model, in the region where the Nazca Ridge is subducting. The smooth and optimal models are similar and both show a second region of afterslip (region B) located near the epicenter as well as a region of slip reversal (region C) corresponding approximately to the rupture area of the Pisco Earthquake.

Figure S8 shows, for the interseismic model, the moment rate and reduced chi-square as a function of the smoothing parameter. Our optimal model corresponds to γ=2.5. We define the range of acceptable models such that the rougher of our models corresponds to γ=0.25 while γ=25 for the smoother model. All acceptable models show that the area corresponding to the subduction of the Nazca ridge corresponds to a region of low *ISC*.

Text S5. Coseismic distribution

Our preferred coseismic model obtained considering a smoothing parameter of 2 (see Text S4 for a justification of this value) and a fixed slip azimuth of N250E° shows a single asperity of high slip (Fig. S7). Observed and predicted coseismic displacements and residuals are plotted in Figure S1. For most interferograms, χ^2_r is generally close to 1, except for the ENVISAT track 447 for which χ^2_r=2.5. This larger discrepancy is presumably due to an underestimation of observational errors and could be explained by the poor and heterogeneous coherence near Pisco City, complicating phase unwrapping. Another possible cause is an atmospheric phase delay due to variability in tropospheric water vapor concentration in the study area [*Remy et al.*, 2011].

The major coseismic slip is located offshore the Paracas Peninsula with a maximum slip of about 10 m at 20 km depth. Independently of the roughness value chosen (Figure S6a-c in supporting information), the largest amount of coseismic slip occurs near the Paracas peninsula (Figures 6 and S9). In the case of the rough model (γ=0.2), the slip distribution is characterized by a large asperity offshore the peninsula and an elongated area of lower coseismic slip northward. Our preferred coseismic model is very similar to the one presented by *Pritchard and Fielding* [2008]. It is also similar to the one proposed by *Sladen et al.* [2010]. A major difference though is that *Sladen et al.* [2010] derived two slip patches, one close to the epicenter location, and a second larger one, in the same area as our peak slip. The two asperities are not resolvable with the InSAR data only and hardly show up for rough slip distributions (Figure S6 in supporting information). Our slip distribution model does not show an updip extension as the ones proposed by *Motagh et al.* [2008] and *Biggs et al.* [2009]. In our model, slip is penalized in this area due to the poor resolution of the InSAR data.

Text S6. Existence of the Slip reversal Region

Considering the non-uniqueness of the underdetermined inversion problem, we discuss here the robustness of the existence of the afterslip in backward direction observed at region C of Figures 6a-c, 7d and 9d. Clearly, this region appears only in the GPS based models and it is not present on the InSAR based model of Figure 6b. The model in Figure 6b well adjusts the InSAR data (χ^2_r of 0.70) without requiring for slip reversal in region C. This is understandable since region C stands in a low-resolution area as might be seen looking at Figure 5b. Furthermore, deformation induced by a moderate amount of slip in region C would be hidden in InSAR data that are mostly sensitive to the large afterslip patch of region A. Next, we performed an inversion of the GPS data alone penalizing slip in region C where slip reversal is observed. When slip is penalized in region C (Figure S10) , the model predicts χ^2_r =1.90 instead of 0.7 (when slip reversal is allowed in region C). This significant difference is mainly explained by the large discrepancies between observed and modeled displacements at ENAP, in particular in the east-west component. Therefore the existence of some amount of slip reversal in region C is required to properly adjust the GPS data and does not result from a lack of resolution.

Text S7. Estimate of the Total Postseismic Moment

The GPS data span a time period extending from days 20 to 1220 after the mainshock. Let us assume that the postseismic moment evolves as

$$M0_{post}(t) = \alpha f(t,\beta) \quad , \qquad \text{(E1)}$$

where α is a constant, t the time following the mainshock and β some parameters.
Let us call t_1 and t_2 two epochs such that $t_2 > t_1$. Using Eq. (E1) we can relate $M0_{post}(t_1)$ to $M0_{post}(t_2)$ yielding

$$M0_{post}(t_2) = M0_{post}(t_1)\frac{f(t_2,\beta)}{f(t_1,\beta)} \quad , \qquad \text{(E2)}$$

Let us define $\Delta M0_{post}$, the postseismic moment accumulated between t_1 and t_2

$$\Delta M0_{post} = M0_{post}(t_2) - M0_{post}(t_1) \quad , \qquad \text{(E3)}$$

Combining Eq. (E2) and (E3) finally gives

$$M0_{post}(t_2) = \zeta(t_1,t_2)\Delta M0_{post} \quad , \qquad \text{(E4)}$$

where $\zeta(t_1,t_2)$

$$\zeta(t_1,t_2) = \frac{1}{1-\frac{f(t_1,\beta)}{f(t_2,\beta)}}, \qquad \text{(E5)}$$

Assuming frictional afterslip as the dominating process for postseismic relaxation yields the particular form of $f(t,\beta)$

$$f(t,\beta) = \log[1 + d(\exp(t/t_r) - 1)], \qquad \text{(E6)}$$

in agreement with Eq. (8).
Taking t_1=20 days, t_2=1204 days, d=188 and t_r=2.26 yr as found in section 6.1 yields $\zeta(t_1,t_2) \approx 1.37$. Consequently, the total postseismic moment between days 0 and 1204 is 1.37 times larger than our inverted postseismic moment estimated between days 20 and 1204.

Table S1. Comparison between InSAR and GPS data

ENVISAT track 354		
GPS station	**GPS (cm)**	**InSAR (cm)**
LAGU	-2.0	-2.6
ENAP	-1.7	-1.1
ALOS track 111 (25/08/2007-29/05/2008)		
LAGU	-9.3	-10.5
ENAP*	-3.7	-5.1
ALOS track 111 (25/08/2007-17/07/2009)		
LAGU	-11.7	-12.3
ENAP*	-3.4	-4.5
ALOS track 111 (25/08/2007-01/09/2009)		
LAGU	-11.6	-12.6
ENAP*	-4.3	-3.7
ALOS track 110 (25/09/2007-12/05/2008)		
GUAD	-0.9	-0.9
ALOS track 110 (25/09/2007-30/06/2009)		
GUAD	-0.4	-1.8

*means that InSAR value from the interferograms formed with the master image acquired 12 days after the earthquake is compared with the GPS values acquired at ENAP days 14 after the earthquake.

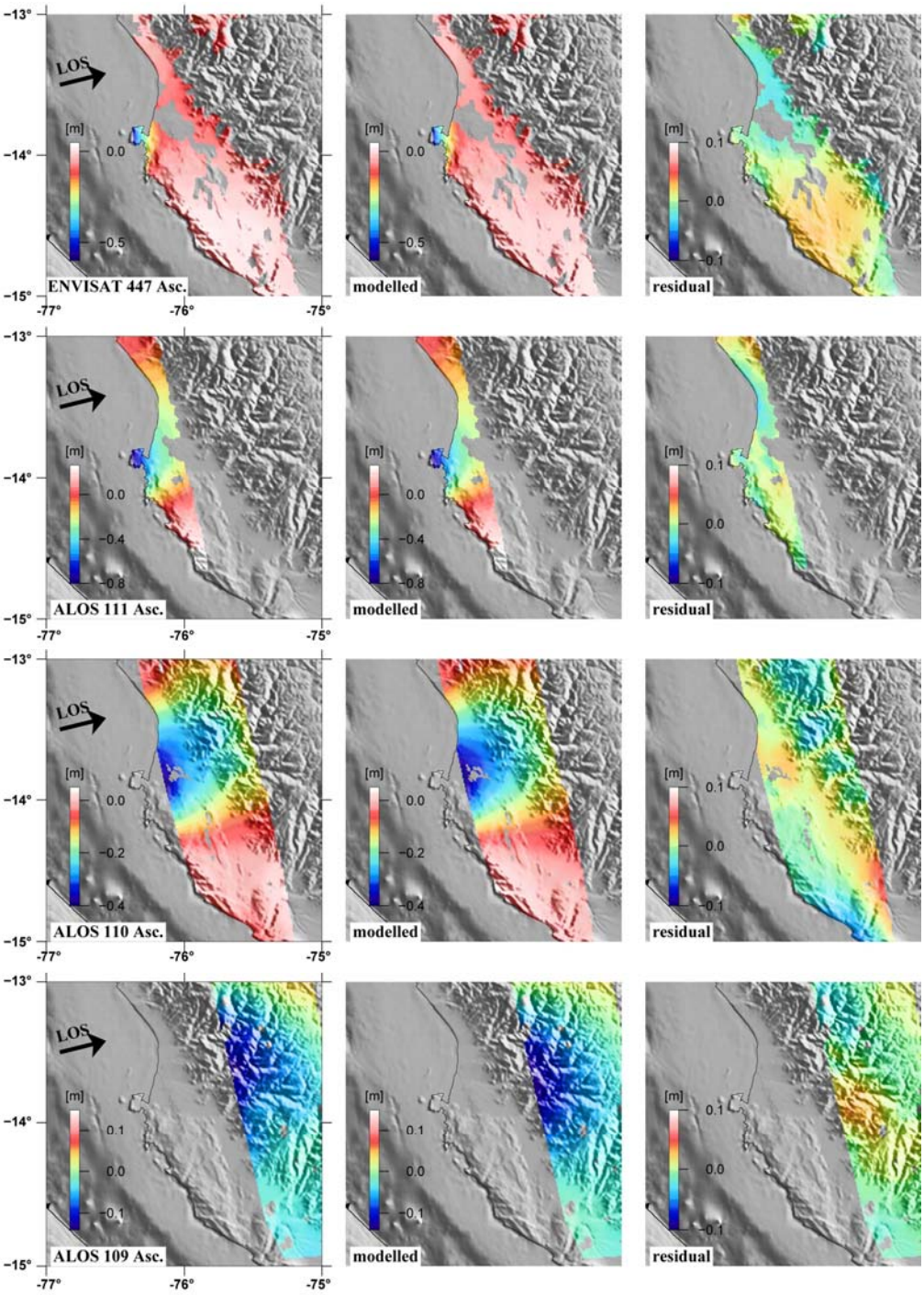

Figure S1. Observed and modeled coseismic interferograms for the Pisco earthquake. The satellite to ground radar line-of-sight is shown with a black arrow. The largest InSAR displacement observed is about 0.85 m from ALOS interferogram acquired in track 111. The fit between predicted and observed interferograms is generally good with a χ^2_r close to one except for the ENVISAT track 447 (χ^2_r=2.5). Note that different color scales are used for better readability. Displacements toward the satellite are negative.

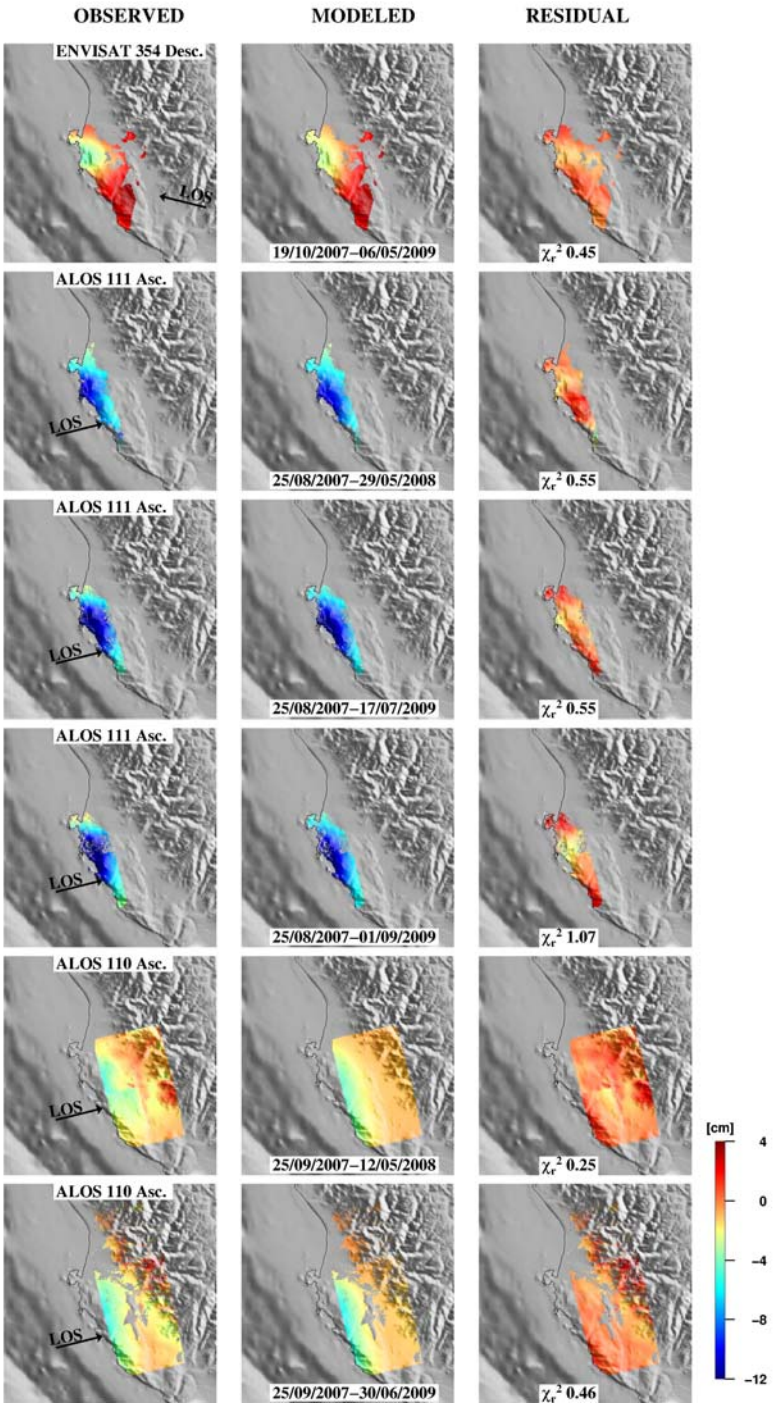

Figure S2. Observed and modeled postseismic interferograms. The satellite to ground radar line-of-sight is shown with a black arrow. Displacements toward the satellite are negative.

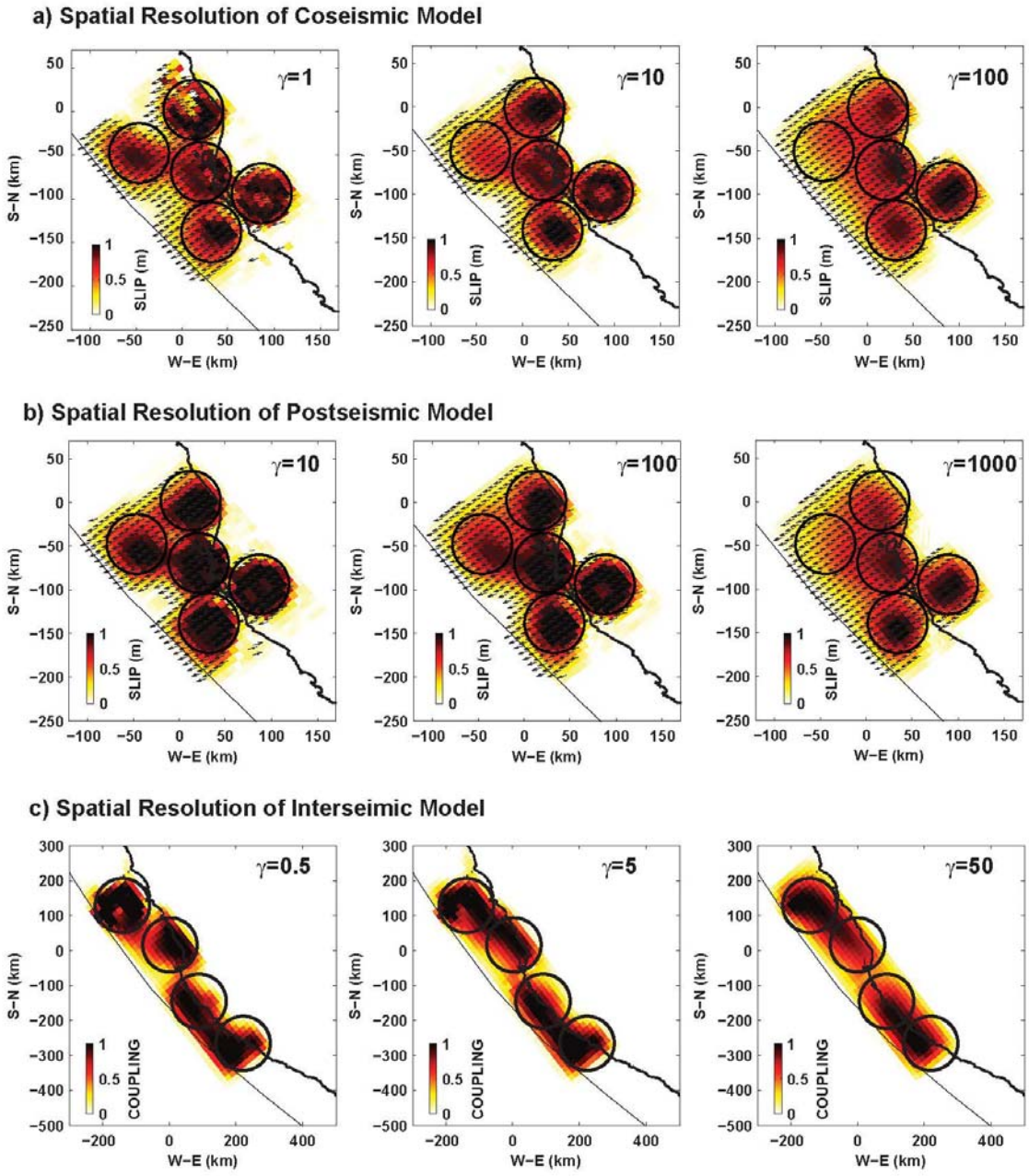

Figure S3. Resolution tests for the co-, post- and interseismic fault models considering a pattern of circular asperities. **a**) Resolution test for the coseismic model considering a pattern of circular asperities of radius=35 km. **b**) For the postseismic model considering a pattern of circular asperities of radius=35 km. **c**) For the interseismic model considering a pattern of circular asperities of radius =70 km

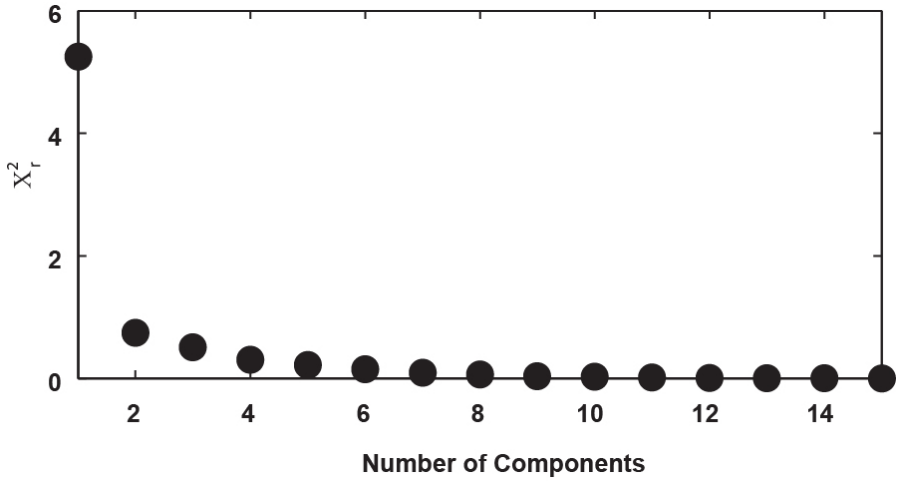

Figure S4. Reduced chi-square of the residual between the observed and reconstructed time series as a function of the number of components of the PCAIM decomposition.

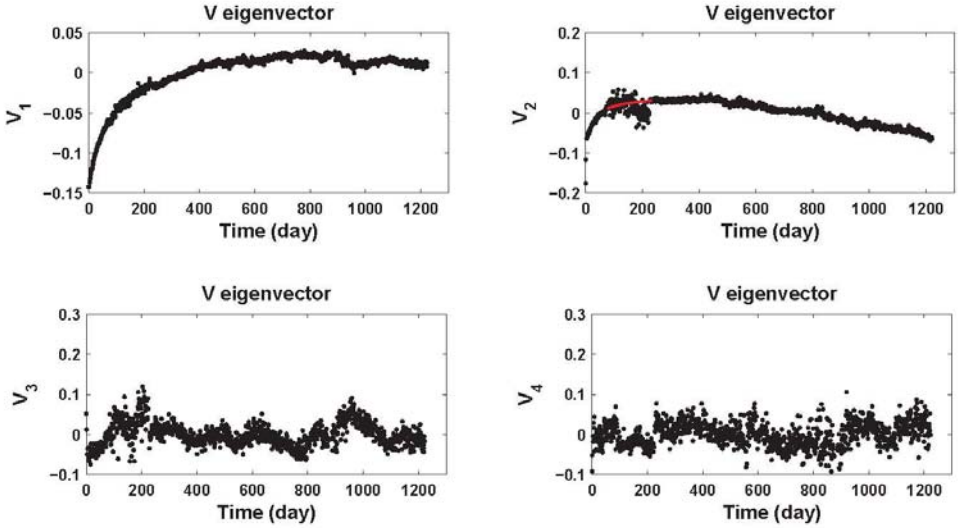

Figure S5. Temporal eigenvectors for the first four components.

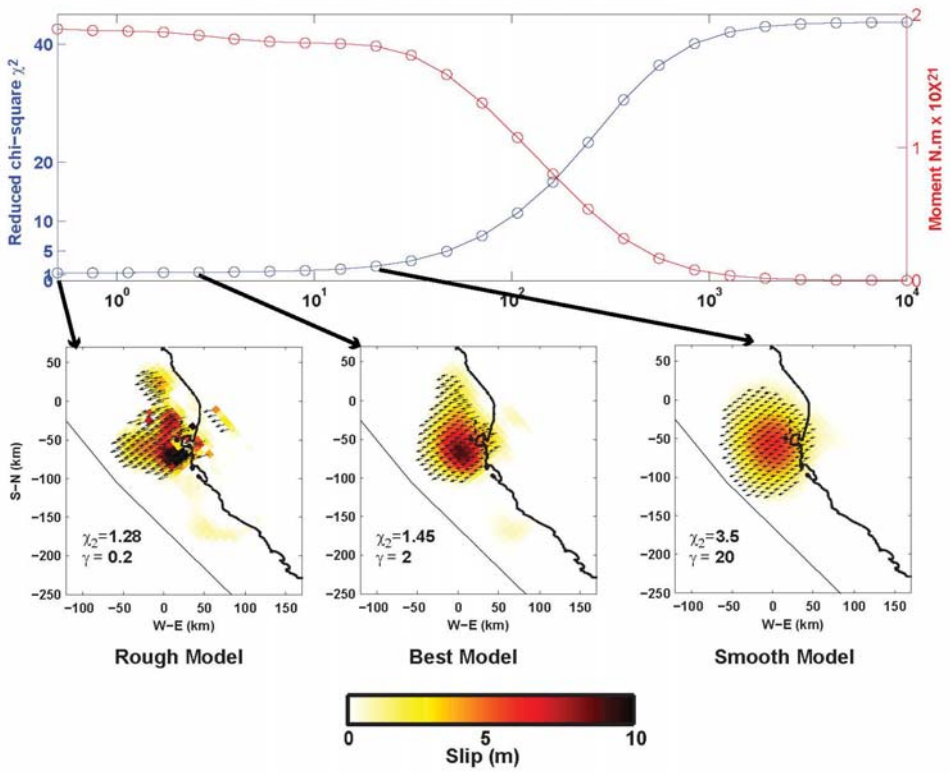

Figure S6. **a**) Reduced chi-square and seismic moment as a function of the smoothing parameter γ for the coseismic model. **b**) Coseismic slip distribution models for three different values of the smoothing parameter (0.2, 2 and 20).

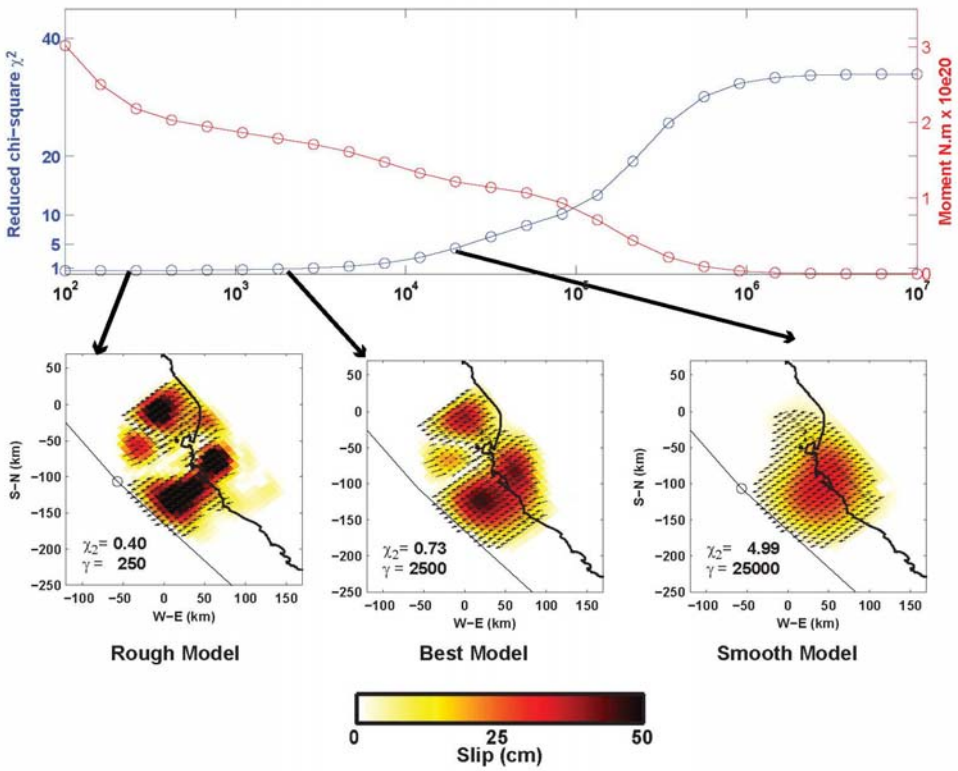

Figure S7. a) Reduced chi-square and seismic moment as a function of the smoothing parameter γ for the postseismic model. **b**) Postseismic slip distribution models for three different values of the smoothing parameter (250, 2500, 25000).

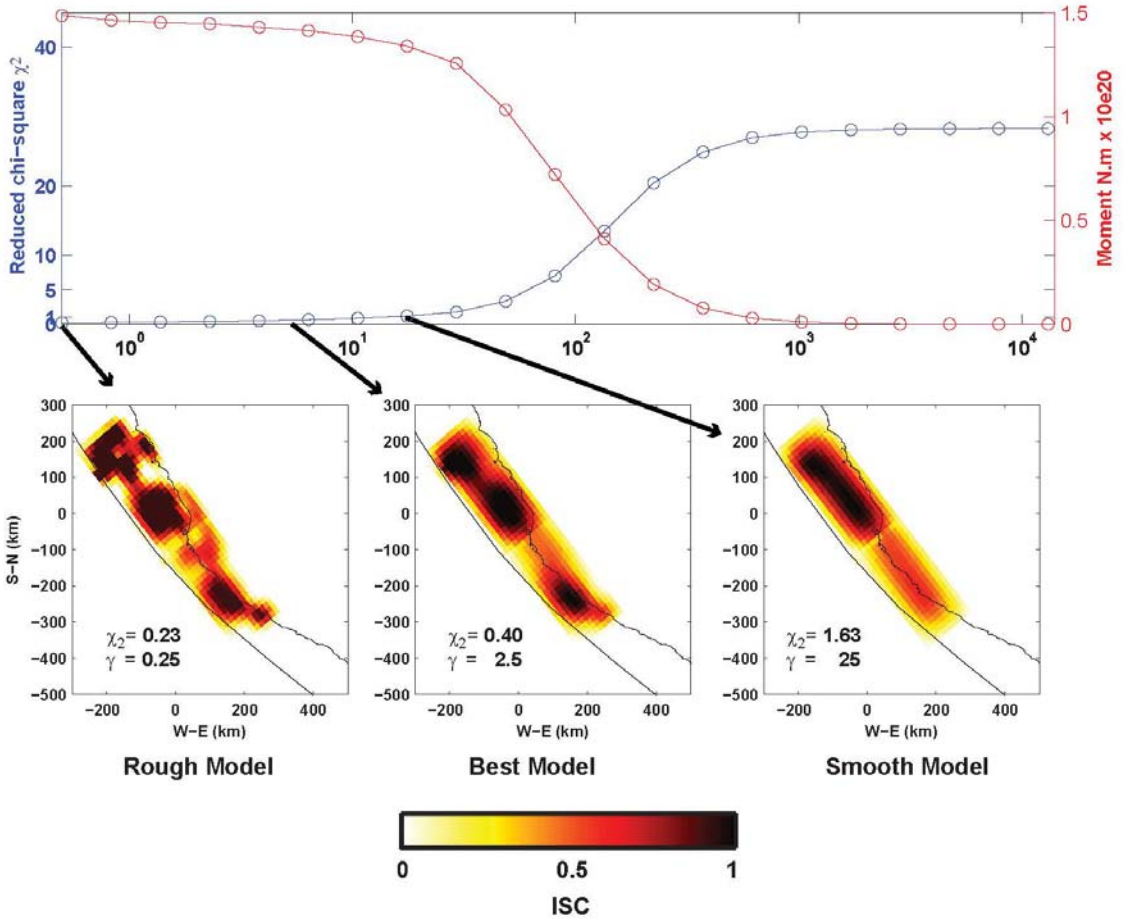

Figure S8. a) Reduced chi-square and moment rate deficit for GPS data including 4 mm/yr of back-arc shortening as a function of the smoothing parameter γ. **b**) Interseismic slip distribution models for three different values of the smoothing parameter (0.25, 2.5, 25).

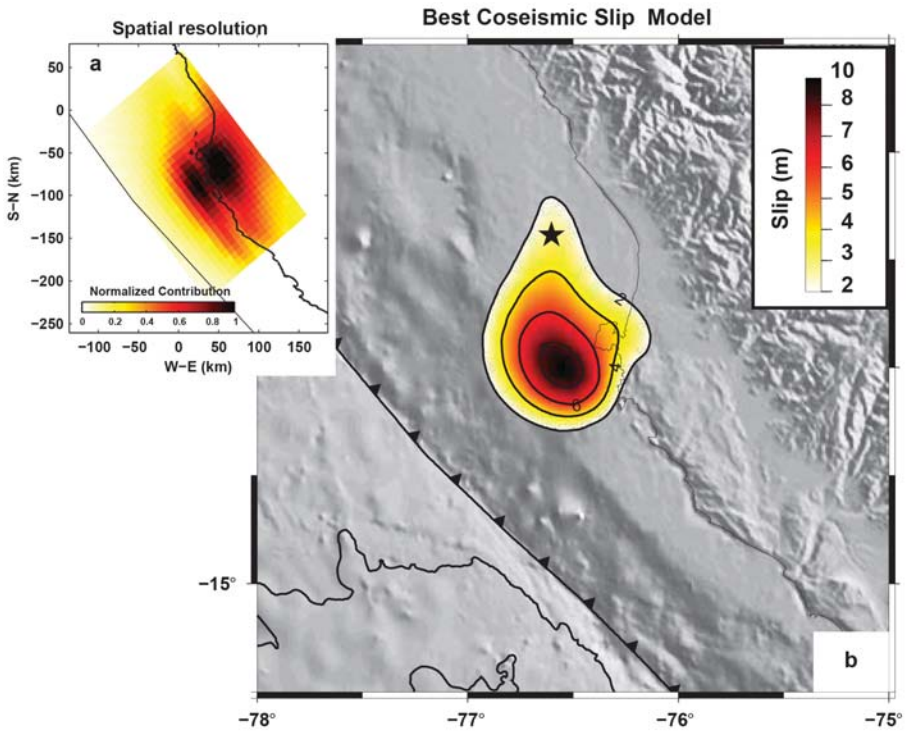

Figure S9. a) Normalized contribution of each patch to the total displacement of coseismic interferograms assuming a homogeneous slip with an azimuth fixed to 200°SSW. **b**) Best coseismic slip distribution model inferred from InSAR data. The low resolution areas (value < 0.1) in figure S7.a and represented by the gray transparent area in figure S7.b are used to constrain the coseismic slip distribution model. The black star shows the hypocenter location from NEIC.

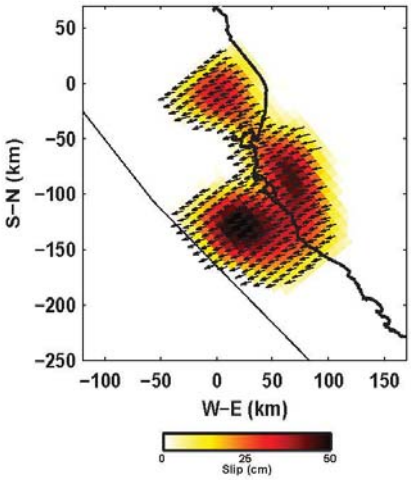

Figure S10. Slip Distribution model obtained by penalizing slip in the region where back-slip is observed (region C). This model poorly explains the GPS data leading to a χ^2_r of 1.80.

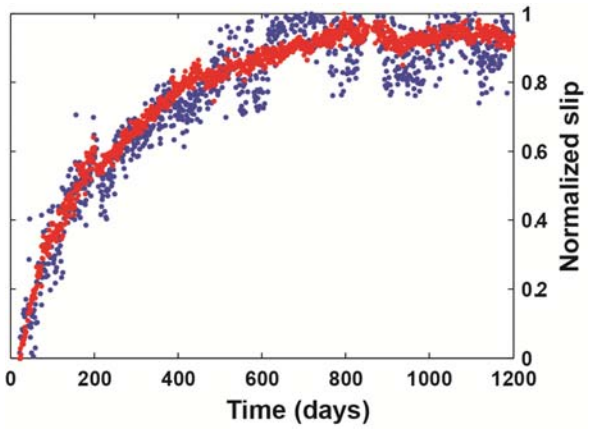

Figure S11. Normalized slip at the center of patches B (in red) and C (in blue). The temporal evolution of slip is similar in both patches and only the slip amplitude is different at site B, that shows a large amount of afterslip.